

# Investigation of fatigue crack incubation and growth in cast MAR-M247 subjected to low cycle fatigue at room temperature

Saikumar R. Yeratapally · Jacob D. Hochhalter  · Timothy J. Ruggles · Michael D. Sangid

Received: 27 December 2016 / Accepted: 19 April 2017 / Published online: 4 May 2017  
© Springer Science+Business Media Dordrecht (outside the USA) 2017

**Abstract** MC carbide particles (with Hafnium and/or Tantalum as constituent metallic element, M) were observed to crack extensively in a cast polycrystalline nickel-base superalloy, MAR-M247, when subjected to low-cycle fatigue loading at room temperature. High resolution secondary electron images taken on the surface of a double edge notch test specimen revealed that approximately half the carbide particles cracked in the highly-strained notch section of the specimen. These images further illustrated that the average surface area of cracked particles was approximately three times that of the uncracked particles. Additional analysis illustrated that the cracks within a large number of particles aligned nearly perpendicular to the loading direction. However, high aspect ratio particles (with aspect ratio  $>3$ ) were prone to incubate cracks aligned along its major axis, independent of the loading direction. Additionally, forward-scattered imaging often showed a high density of slip bands interaction with most of the particles which cracked. The life limiting crack

growth in MAR-M247 was observed to be crystallographic in nature, as the crack grew along slip bands as measured by high-resolution electron backscatter diffraction, even after spanning many grains. Statistically representative microstructure models of MAR-M247 were generated and used in the crystal plasticity finite element simulations. As expected, there was a significant variation in the computed stress state among constituent carbide particles. The stress state of the carbide particles was found to be heavily influenced by the stress in surrounding grains and the orientation of the major axis of the particles with respect to applied load direction. For particles that intersect the free-surface, stress was found to be highly concentrated at the free surface and a positive correlation between the magnitude of free-surface area and the maximum principal stress was found. Additionally, high stress concentrations were observed in regions where carbide particles intersect grain boundaries.

**Keywords** Nickel-base superalloys · MC carbide particles · Grain boundaries · Forward-scattered imaging · HREBSD · Crystal plasticity · Microstructure

---

S. R. Yeratapally · T. J. Ruggles  
National Institute of Aerospace, Hampton, VA 23666, USA

J. D. Hochhalter (✉)  
National Aeronautics and Space Administration, Langley  
Research Center, Hampton, VA 23666, USA  
e-mail: jacob.d.hochhalter@nasa.gov

M. D. Sangid  
School of Aeronautics and Astronautics, Purdue University,  
West Lafayette, IN 47907, USA

## 1 Introduction

Cast MAR-M247 is a polycrystalline nickel-base superalloy well known for its high temperature strength, ductility, fatigue and creep resistance (Nathal et al. 1982). Grain boundary strengthening and enhance-

ment of ductility at high temperatures is achieved in MAR-M247 through the formation of discrete MC carbide particles (with B1 lattice structure and constituent metallic element, M, being Hafnium/Tantalum) and  $M_{23}C_6$  carbide particles (with FCC lattice structure and constituent metallic element, M, being Chromium) during solidification (Chen et al. 1998) and thermal aging processes (Janowski 1985), respectively. The mechanical properties of MAR-M247 are greatly dependent on the size, morphology, volume fraction, and distribution of the carbide particles within the matrix of the material (Gell and Leveran 1968; Kotval et al. 1972; Kaufman 1984).

Several studies have aimed at characterizing the microstructure and identifying the mechanisms of crack initiation and growth in polycrystalline MAR-M247 (Kotval et al. 1972; Wawro 1982; Kaufman 1984; Boismier and Sehitoglu 1990; Bor et al. 1999; Szczotok et al. 2006; Szczotok and Rodak 2012; Šmíd et al. 2014, 2016). While the Chromium rich  $M_{23}C_6$  particles present at the grain boundaries help resist grain boundary sliding and increase ductility at high temperature, previous studies have found that brittle cracks initiated and contributed in providing a preferred path for crack propagation at the elongated Hafnium and Tantalum rich MC type carbide particles (Kotval et al. 1972; Wawro 1982). Several studies have used high-resolution electron backscatter diffraction (HREBSD) to calculate the evolution of dislocation density, residual stresses, thermal and mechanically induced strains in the vicinity of non-metallic inclusions in nickel-based superalloys (Karamched and Wilkinson 2011; Zhang et al. 2014, 2016, 2015; Jiang et al. 2015). Although microscopy imaging, coupled with HREBSD technique provides valuable information regarding the deformation mechanisms leading to crack incubation and initiation, along with the quantified state of micromechanical deformation in the vicinity of carbide particles, they do not provide information regarding the complex 3D stress state of the particles, and the surrounding grains.

For early engineering applications, the effects of microstructure on fatigue strength were implicitly considered. For example, efforts were directed toward life prediction models (Sehitoglu and Boismier 1990; Brindley et al. 2015) for MAR-M247 subject to thermo-mechanical loading. Also, the effect of non-metallic inclusions on fatigue strength has been extensively studied with several empirical models now available

(Murakami and Endo 1994). In these foundational studies, statistical distributions of inclusions were used to predict fatigue strength and its scatter. In particular, Murakami and Endo (1994) used the square root of the particle's projected area (normal to its maximum tensile stress direction) as a geometrical parameter to model the effect of inclusion size on fatigue strength. Two inherent assumptions made therein are that inclusions can be regarded as mechanically equivalent to a crack and that the particle size, not shape, is statistically significant.

More recent studies have provided additional insights into the complexities of microstructurally-small crack initiation at inclusions. Bozek et al. (2008) studied a case where only a small percentage (<10%) of all second phase surface particles cracked in AA7075-T651. Therein, crystal plasticity finite element (CPFE) computations were used to illustrate the combined effect of particle aspect ratio, local strain level, and grain orientation surrounding the particle its stress state. Predictions of particle cracking frequency and aspect ratios were in agreement with experiment. Shenoy et al. (2005) studied the effect of neighboring grain orientation on the variation of plastic strain around an inclusion located close to a bi-crystal interface in a nickel-superalloy. Zhang et al. (2009) studied the influence of particle shape and the interface condition between the particle and the matrix in a carburized and shot-peened martensitic steel. Przybyla et al. (2010) studied the change in driving force for nucleation in a near-surface inclusion with the growth in oxide layer on the surface of a martensitic steel. Using gradient-enhanced CPFE, Kartal et al. (2014) calculated the sub-surface residual stresses local to a carbide particle contained in a nickel superalloy single crystal, thereby complementing the free-surface measurements obtained from HREBSD. Salajegheh et al. (2014), using elastoplastic finite element framework, studied how the potency of crack nucleation at a non-metallic inclusion in a martensitic gear steel changes due to the existence of a neighboring inclusion. The aforementioned CPFE studies have provided valuable insights for inclusion-based fatigue crack initiation, mainly in other alloys.

A progression towards modeling increasingly complex details of nickel-based superalloy microstructure has also been made, where much focus has been placed on studying fatigue crack initiation at twin boundaries. Using microstructural computational

models in combination with microscopy data, significant insights have been made into understanding the various factors that act in concert to drive fatigue crack initiation at twin boundaries in various polycrystalline nickel-based superalloys like U720 (Sangid et al. 2011a, b, c), RR1000 (Castelluccio and McDowell 2012; Yeratapally et al. 2016), LSHR (Cerrone et al. 2015) and René 88DT (Miao et al. 2009). In contrast, fatigue crack initiation in cast MAR-M247, which does not have twin boundaries, occurs at MC carbide particles. A similar study towards understanding various factors that contribute to MC carbide particle cracking, specifically in cast polycrystalline nickel-based superalloys like MAR-M247 is warranted.

In the current work, microscopy data (secondary electron and forward-scattered electron imaging) combined with EBSD analysis was used to characterize the statistics of crack incubation sites, and micromechanics of deformation in the vicinity of cracked particles. Further, fatigue experiments and microscopy analysis were complemented with microstructural computational models. Virtual microstructures representative of polycrystalline MAR-M247 are used in a CPFPE framework to quantify the variability in the stress state of the carbide particles. These are used to gain insights regarding various factors contributing to the variability in stress state of particles in the microstructure of MAR-M247.

The remainder of the paper is organized as follows. Section 2 discusses the test specimen geometry, fatigue test setup and microstructural characterization of MAR-M247. Section 3 includes results and discussions based on (i) the observations from microscopy scans and (ii) insights learned from CPFPE simulations regarding various factors contributing to the significant variability in stress state within the carbide particles. Conclusions are provided in Sect. 4.

## 2 Fatigue testing and microstructure characterization of MAR-M247

The test specimens of MAR-M247 were sectioned longitudinally from a casting, as shown in Fig. 1a. Using electro-discharge machining, a double edge notch is introduced at the mid-plane of the specimen (as shown in Fig. 1b, c) in such a way that the thickness at the center of the notch is equal to the thickness of a previously proposed thin, high-temperature component, which is used in converting thermal energy into electrical energy on a deep-space mission spacecraft (Bowman et al. 2004; Schreiber and Thieme 2008). The microstructure of the component was produced to obtain optimal high temperature creep and fatigue properties (Wood et al. 2005), which is critical for thin section components.

The double edge notch test specimen was subjected to displacement-controlled low-cycle fatigue testing

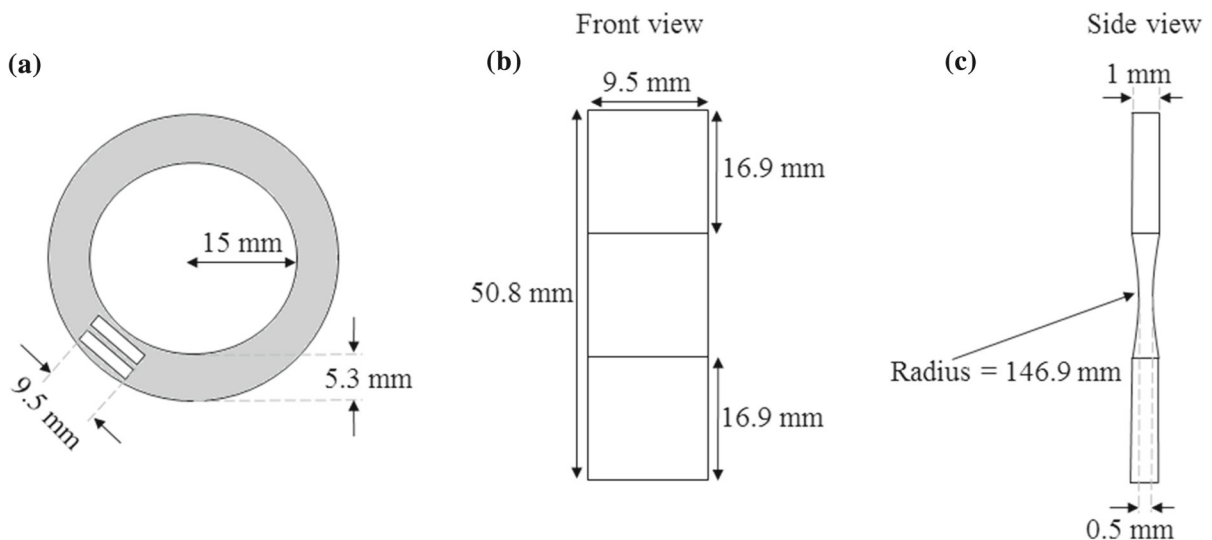


**Fig. 1** a Top view of the casting. Samples were sectioned from the hollow cylinder casting, as shown by the slots in the cylinder. Also shown is b front and c side views of the test specimen with the double edge notch

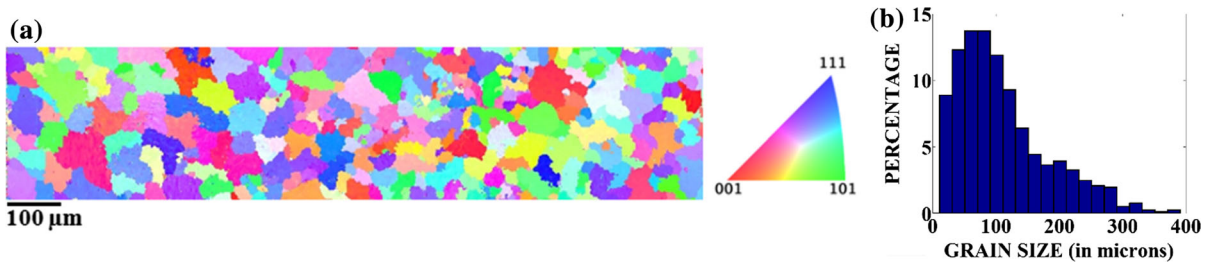


**Fig. 2** **a** EBSD scan of cast MAR-M247 taken in the polished section of the specimen and **b** grain size distribution of cast MAR-M247

at room temperature. Digital image correlation (DIC) was used to determine a peak displacement such that the highest strain in the thinnest section of the specimen was 1.5%. Airbrush was used to deposit titanium oxide paint speckles, which ranged from 10 to 50  $\mu\text{m}$  in diameter. DIC parameters (including magnification, resolution, speckle dimensions, and field of view) were chosen with an intention of capturing macroscopic strain in the region of interest, but not to obtain heterogeneous strains due to the complexities in the microstructure. Based on DIC strain measurements, a peak displacement value of 0.1825 mm was imposed. A stress ratio ( $R$ ) of 0.1 was used to prevent buckling of the specimens. A 10% load drop was used as a fatigue test stop condition to observe cracks on the surface of the sample before failure. Once the fatigue test was stopped, the test specimen was analyzed using a scanning electron microscope to identify and study the crack incubation sites.

The notch area (Fig. 1b, c) was polished in progression of 30–15–6–3–0.5  $\mu\text{m}$  diamond polishing solution followed by 0.05  $\mu\text{m}$  colloidal silica solution to obtain an EBSD quality surface. Subsequently, EBSD scans were obtained over the entire notch width. Figure 2a shows an EBSD scan taken at the notch region of the specimen, while Fig. 2b shows the grain size distribution of cast MAR-M247 obtained from EBSD data collected at the notch section of the specimen. Grain size distributions obtained from processing the EBSD data are shown in Fig. 2. The average grain size was approximately 110  $\mu\text{m}$ , with the size of the largest grain being 390  $\mu\text{m}$ . Further, it was observed that the material had random texture.

Images were obtained to study the composition and morphology of various types of carbide particles using energy dispersive spectroscopy (EDS) and secondary electron imaging, respectively. It was determined through EDS analysis that the carbide parti-

cles forming a continuous array along grain boundaries were rich in chromium, Fig. 3a. The bulky carbide particles, Fig. 3b, are comprised of Hafnium and Tantalum and are referred to as MC carbides. The coarser MC carbide particles are highly brittle in nature and provide easy paths for rapid crack propagation thereby contributing to the degradation of ductility in the material (Kotval et al. 1972; Wawro 1982).

### 3 Results and discussion

#### 3.1 Observations from electron microscopy

Results of the EDS analysis and microscopy observations illustrated that carbide cracking occurred exclusively at Hafnium/Tantalum MC carbides in the notch section. Consequently, the remainder of this study was focused on crack incubation in Hafnium/Tantalum MC carbide particles. Secondary electron images of 150 particles (80 uncracked and 70 cracked particles) were collected to determine correlations between their geometry and cracking. Geometric attributes considered were the free surface area, aspect ratios (calculated as the ratio between length of major and minor axis of a best fit ellipse), and the angle made by the crack (within the cracked particle) with respect to the loading direction. All of the aforementioned metrics were collected using an open source image processing and analysis software, ImageJ (Schneider et al. 2012).

A correlation was found between particle cracking and the area of the particle on the surface of the specimen. Figure 4 compares the free-surface area of cracked and uncracked carbide particles as cumulative probabilities. The average free-surface area of cracked carbide particles was approximately three times that of the average free-surface area of particles that were still intact. This increased probability of crack incubation in particles with greater free-surface area can be attributed to

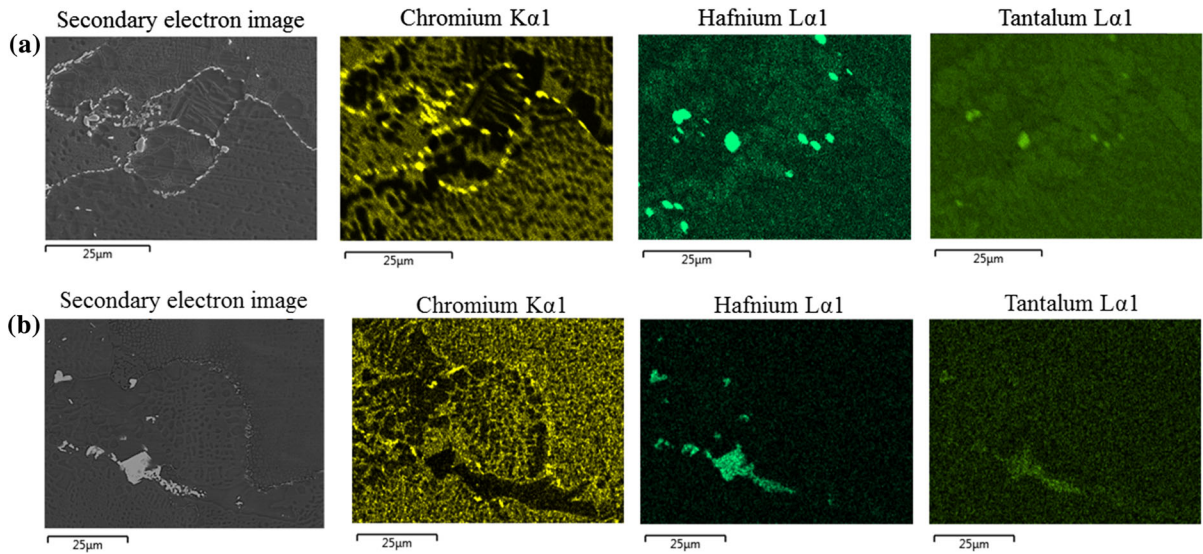


**Fig. 3** **a** Secondary electron image and EDS analysis showing Chromium rich  $M_{23}C_6$  particles which preferentially formed along grain boundaries. Also evident are a few scattered Hafnium and Tantalum rich particles that are larger than the Chromium rich

$M_{23}C_6$  carbide particles. **b** Secondary electron image and EDS analysis of a bulky MC carbide particle shows that the particle has a high composition of Hafnium and Tantalum

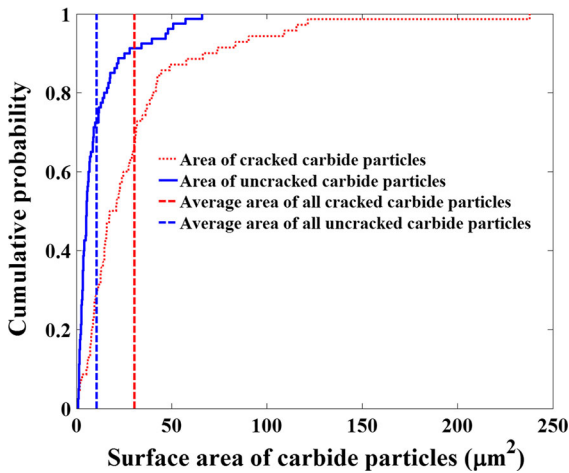


**Fig. 4** Overlay of cumulative distributions of free-surface areas of cracked and uncracked carbide particles

many factors acting in concert, including but not limited to higher driving stress and increased interaction with slip bands resulting in the formation of more pileups at the intersection sites of the particles and slip bands.

Approximately 10% of the particles that have free-surface area greater than the average free-surface area of cracked particles remained intact, see Fig. 4. From surface observations alone, it was not possible to unambiguously determine why some apparently-large par-

ticles did not crack. Availability of 3D data would help clarify any sub-surface effects that influence crack incubation in carbide particles. However, due to lack of 3D data in the current study, synthetic 3D microstructures (discussed in Sect. 3.3) are instead used to determine various contributing factors to crack incubation in these particles.

The angles made by several cracks with the loading direction,  $\theta$ , is plotted as a histogram in Fig. 5a. It is evident that most of the cracks aligned almost perpendicular to the loading direction. This is particularly true for most of the low aspect ratio (aspect ratio  $< 3$ ) carbide particles. The cracks in high aspect ratio particles are not perpendicular to the loading direction (Fig. 5a). In these particles, cracks preferentially formed along the major axis of the particle. This behavior is illustrated in Fig. 5b, which shows a low- and high-aspect ratio cracked carbide particle and angles made by the cracks with respect to the loading direction. From Fig. 5b, it can be seen that in the low aspect ratio carbide particle, the crack formed is almost perpendicular to the loading direction, whereas in the high aspect ratio particle, the crack is aligned along its major dimension.

Additionally, forward-scattered imaging was used to capture the topographic contrast, which reveals information of slip bands in the local neighborhood of the

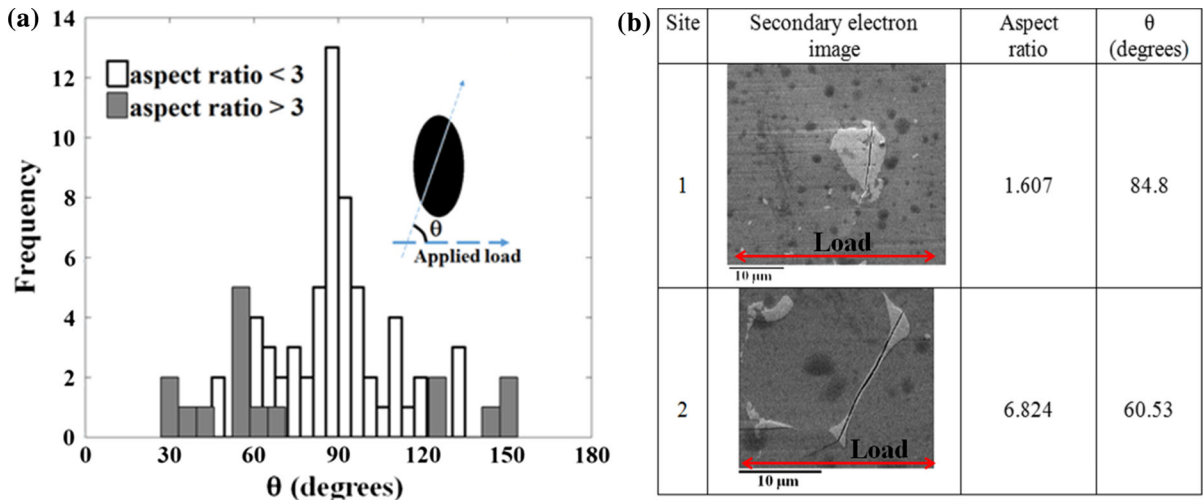


**Fig. 5** **a** Overlay of two histograms, with one showing the angles measuring the inclination of cracks (with the load direction) formed within 54 different carbide particles with aspect ratios less than 3, and the other histogram showing angles measuring the inclination of cracks (with the load direction) formed in 16

carbide particles with aspect ratio  $> 3$ . A schematic of a cracked carbide particle is also shown to indicate the measurement of  $\theta$ , the angle between crack and applied load. **b** Sites 1 and 2 show a low aspect ratio and a high aspect ratio cracked carbide particles, respectively

cracked particles. Forward-scattered electron images were taken in the vicinity of 40 particles (out of the 150 particles whose size and shape metrics were evaluated from secondary electron images) to investigate the presence of slip bands. The interaction of slip bands with cracked carbide particles can be clearly observed in the forward-scattered images shown in Fig. 6. The interaction between slip bands and the brittle carbide particle causes dislocations to pile-up at the interaction sites, locally raising the stress within the carbide particle.

Slip bands were not observed at every cracked carbide particle. There were also cases where slip bands were observed at carbide particles that did not incubate cracks in particles. Based on these observations it can be inferred that, although it is likely that the slip bands on carbide particles influence the propensity of crack incubation, it is not a necessary condition for the observed carbide particle cracking. Table 1 summarizes these observations. A specific example of each case in Table 1 (except for case including both slip band interaction and cracked particles as shown in Fig. 6) is shown in Fig. 7.

EBSD scans were taken in the vicinity of cracked carbide particles (as shown in Fig. 8). The cracking of particles located at grain boundaries could be driven

due to localized elastic stress concentrations at grain boundaries. Localized elastic stresses arise due to significant differences in the elastic modulus of grains on either side of a grain boundary (Margolin 1998; Neumann 1999). In the current scenario, high localized stresses arise at the interface of the carbide particles with neighboring grains as there is lack of symmetry in crystal structure (between MC carbide particle and surrounding grains). Also, there is a significant difference in elastic moduli between anisotropic grains (with cubic elastic constants  $C_{11}$ ,  $C_{12}$  and  $C_{44}$  equal to 258.6, 167.0, 125.0 GPa respectively (Kuhn and Sockel 1988), and MC carbide particles (with cubic elastic constants  $C_{11}$ ,  $C_{12}$  and  $C_{44}$  equal to 480.0, 103.0, 177.0 GPa respectively (Kamış et al. 2011).

### 3.2 Crystallographic crack growth in MAR-M247

Out of the 70 cracked particles that were investigated, in only 10 cases did the cracks initiate, i.e. grow into the matrix, and of those, 4 of them grew in an unambiguously crystallographic fashion, as shown in Fig. 9. Examination of the life-limiting crack in the specimen, Fig. 10, showed the presence of cleaved carbides in the crack path. This life-limiting crack spanned over ten coarse grains. An EBSD analysis of the tip

**Fig. 6** Secondary electron image and forward-scattered images of the neighborhoods of three cracked carbide particles. Forward-scattered images show the topology of the cracked carbide particles,  $\gamma-\gamma'$  matrix surrounding the particle and the slip bands interacting with the carbide particles. In order to add further clarity regarding slip bands, two slip band traces are displayed using *red lines* in site 1. The loading direction and specimen axis are horizontal for all images

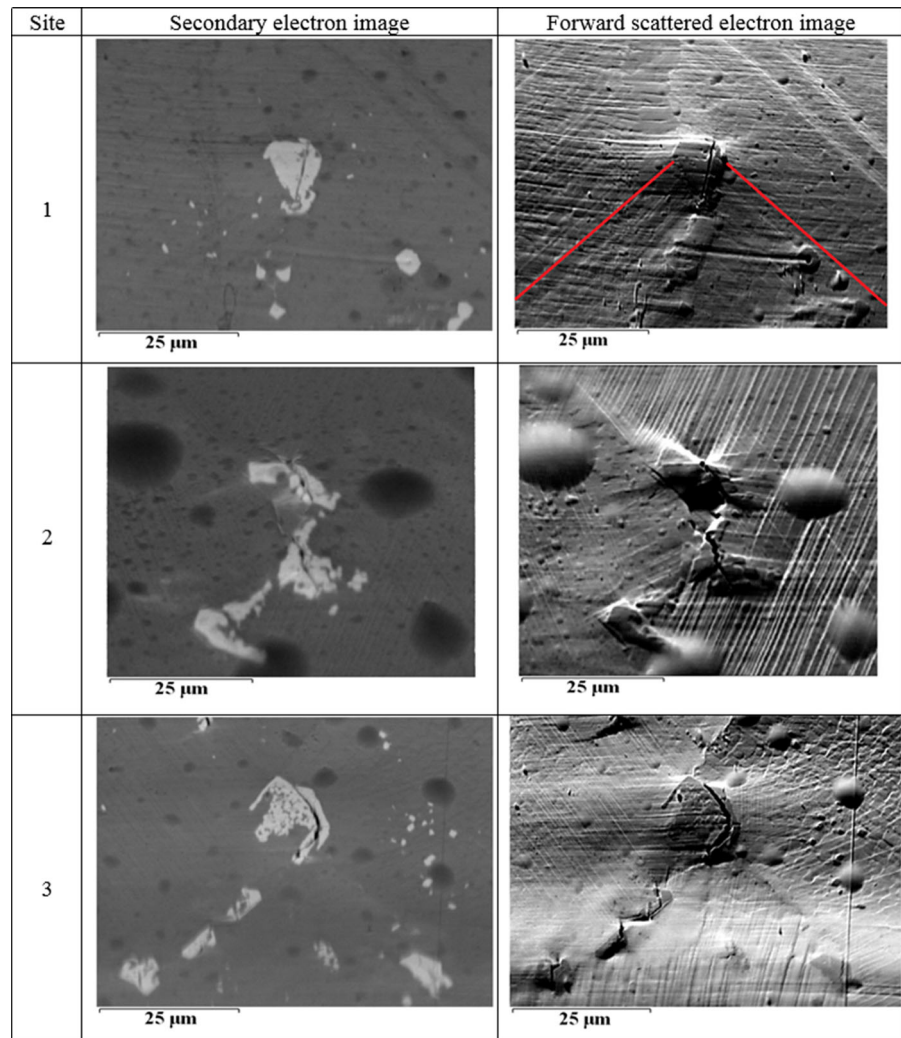


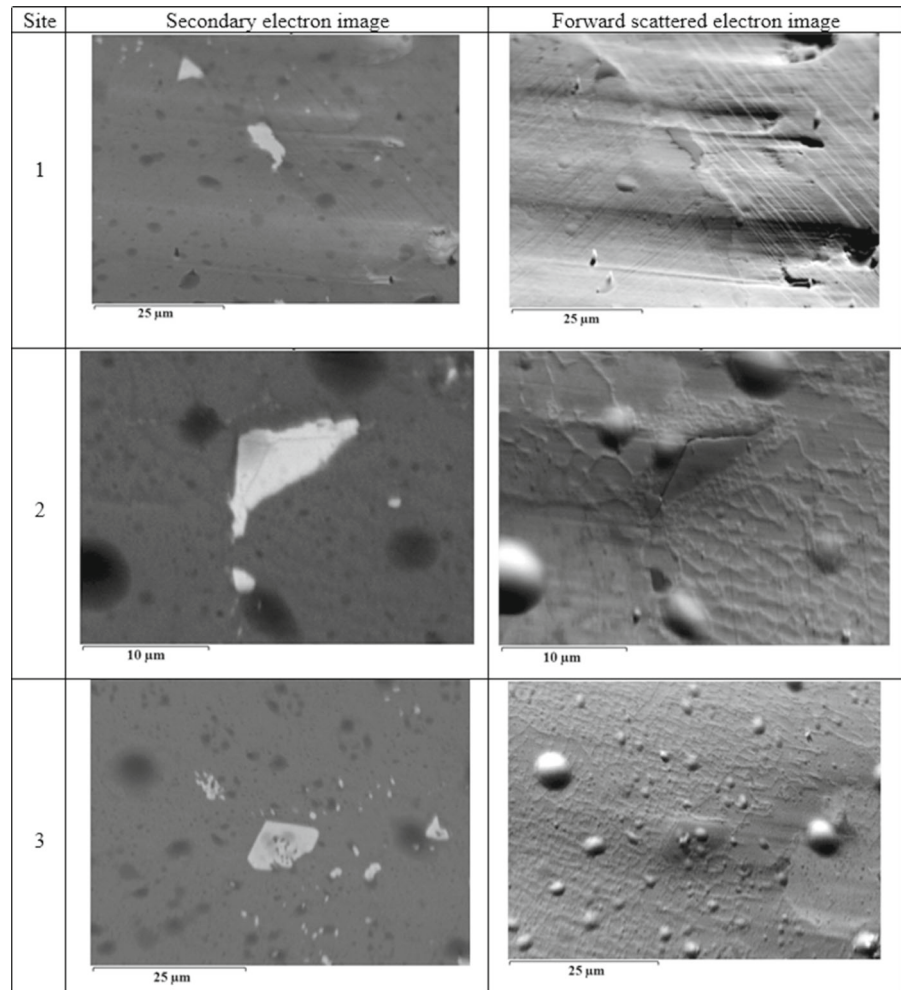
**Table 1** Data obtained regarding interaction of slip bands and particle cracking based on the investigation of forward-scattered images collected at 40 different particles in the highly strained region of the specimen

Slip band interaction	Number of cracked particles	Number of uncracked particles
Yes	29	3
No	4	4

of this macroscopic crack shows that crystallographic cracking continues, suggesting that crack growth is largely crystallographic at all stages of fatigue crack growth. To show how the crack growth lines up with

localized deformation features, high resolution EBSD (HREBSD) post processing was performed at this tip of the life-limiting crack (Ruggles et al. 2016). HREBSD analysis provides a map of geometrically necessary dislocation structure at the same length scale as the EBSD scan. Slip traces of the two slip planes involved in the cracking, the  $(\bar{1}\bar{1}1)$  and the  $(11\bar{1})$ , are shown on an HREBSD dislocation density map around the crack tip in Fig. 11. The dislocation density is not homogeneously distributed, but rather accumulates into geometrically necessary boundaries and slip bands with similar saturation values of dislocation density (around  $2.5 \times 10^{14} \text{ m}^{-3}$ ). From this dislocation density map shown in Fig. 11, it appears that plastic deformation ahead of the crack tip accumulates in the form of slip bands that facilitate crack growth. Crystallographic

**Fig. 7** Secondary and forward-scattered electron images of 1 an intact carbide particle at a grain boundary interacting with slip bands, 2 a cracked carbide particle with no trace of slip band interaction, and 3 an intact carbide particle with no trace of slip band interaction



crack growth, even at a point when the crack has passed through several grains suggests that it is inadequate to use any crack growth model (for thin-walled specimens made of cast MAR-M247) that does not take into account the microstructure of the material. This extended crystallographic growth could be a result of the extremely thin specimen at the notch.

### 3.3 Crystal plasticity analysis to statistically study the stress state of carbide particles

It was evident from microscopy observations that not all the visible carbide particles cracked, cf. sites 1 and 3 shown in Fig. 7. To predict crack incubation frequency for this material in service, it is of interest to understand the fundamental reasons why some particles are more vulnerable to crack incubation than

other particles. Although microscopic imaging coupled with EBSD provided valuable information to correlate carbide geometry and qualitative deformation mechanisms leading to crack incubation, it cannot provide information regarding the complex 3D stress state of the particles, and the surrounding grains. To study the complex stress state in particles, it is necessary to model the heterogeneous microstructure surrounding the carbides.

For this purpose, a CPFE framework was used to statistically study the stress state of the carbide particles. Synthetic microstructure realizations were created using DREAM.3D (Groeber and Jackson 2014), based on the statistics of the microstructures: texture and grain size distribution obtained from the analysis of EBSD scans and particles sizes obtained from X-Ray computed tomography (CT) data. Based on microscopy



**Fig. 8** Secondary electron images and EBSD maps of the local neighborhood of cracked carbides particles. *Dark spots* visible on the secondary electron image are the speckle pattern applied to the sample for DIC analysis. For all images, the loading axis and the specimen axis are in the horizontal direction

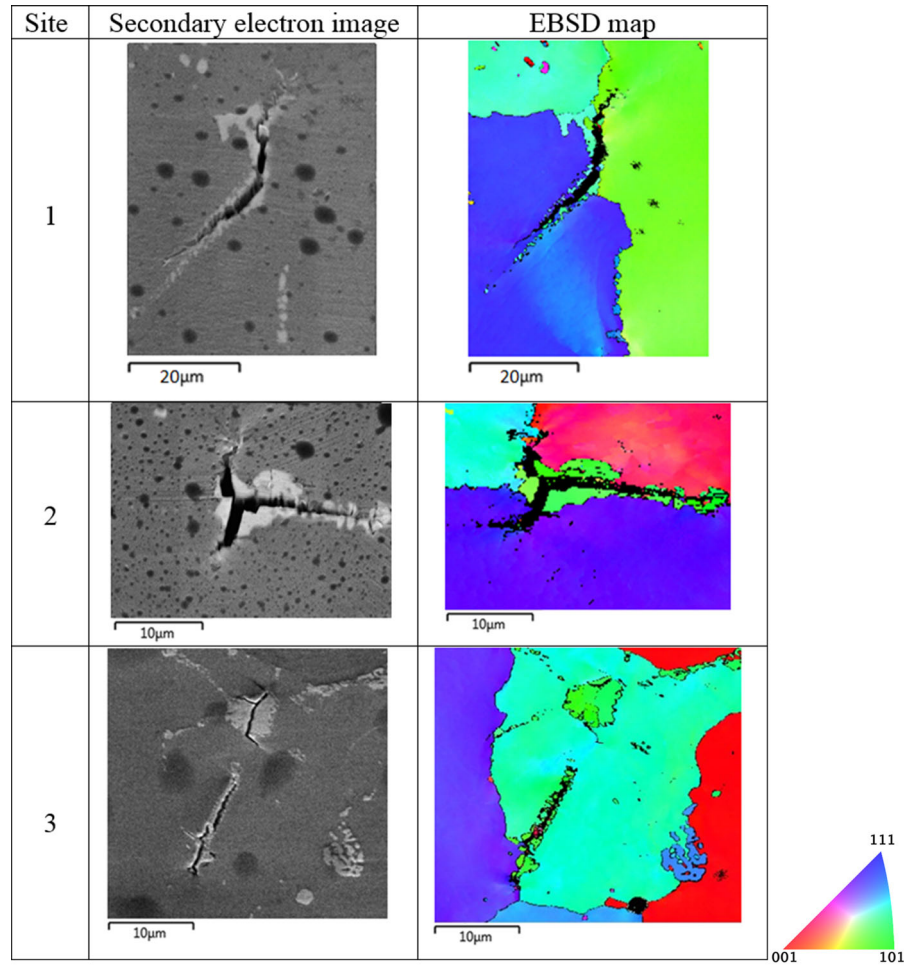
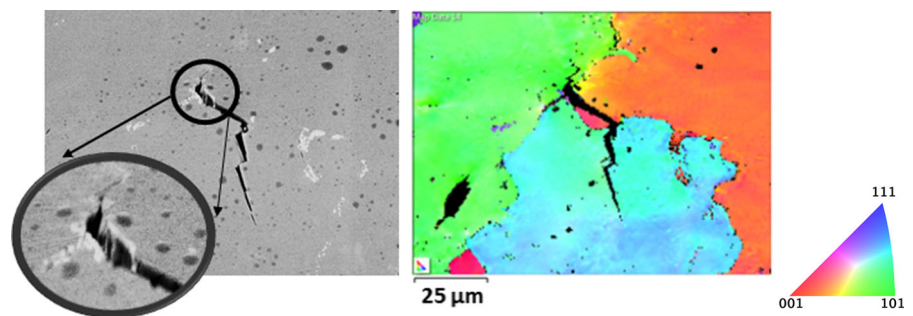


**Fig. 9** Crystallographic crack growth observed for a fatigue crack that initiated within carbide. The location of the carbide is shown using a *circle*. The loading direction is *horizontal*



observations, there was no evidence that second-order geometrical irregularities present on carbide particles specifically influenced cracking in particles. Hence, for the purpose of the current study, while modeling MC carbide particles in microstructures, the second-order geometrical features (irregularities) were not considered, and the MC particles were modeled as smooth ellipsoidal geometries. A moment invariant parameter,

$\bar{\Omega}_3$ , in the 'StatGenerator' toolbox of DREAM.3D, was assigned values close to 1, which helps eliminate sharp irregularities on the particles, and dictates the geometry of the particles to be smoother in nature (MacSleyné et al. 2008). Equivalent spherical diameter (ESD) was calculated for all the particles, and was used as a size metric. The mean size of carbide particles was computed to be 9.90  $\mu\text{m}$ , and the largest carbide particle

**Fig. 10** Secondary electron image of a single large crack formed in the notch section of the specimen. Formation of surface extrusions and crystallographic crack growth can be seen in the enlarged images of a crack tip. The loading direction is *vertical*

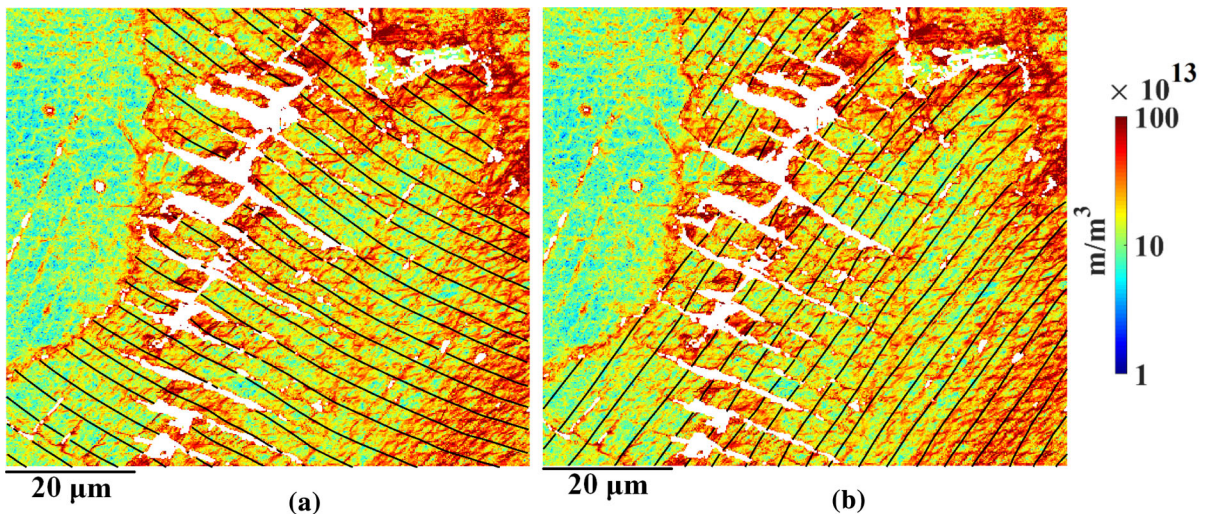
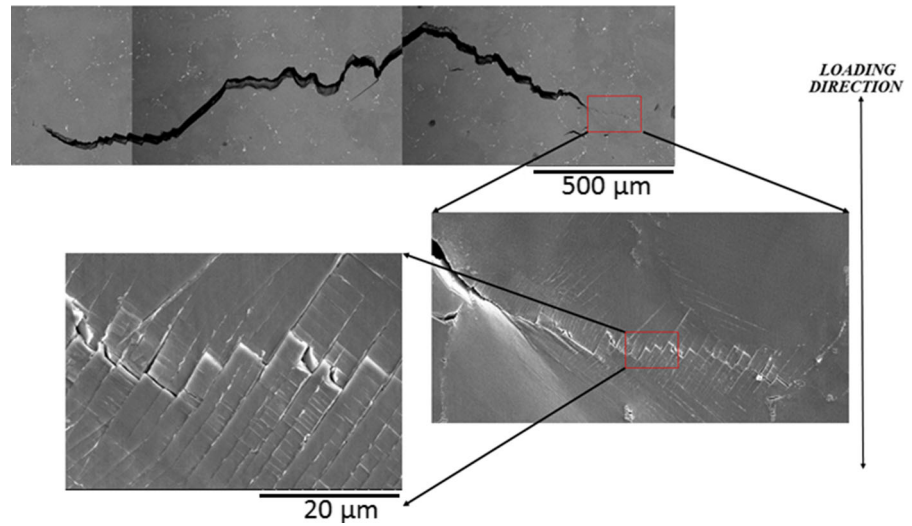


**Fig. 11** Slip traces depicted on a dislocation density map of the region around the macroscopic crack tip for the **a** (111) and **b** (11 $\bar{1}$ ) slip planes. Note that the crack continues to grow crystallo-

graphically along slip bands of these two slip systems. The scale bar of dislocation density (in  $\text{m}/\text{m}^3$ ) is shown in log scale. The cracks are shown in *white*. The loading direction is *horizontal*

had an ESD of  $44.37 \mu\text{m}$ . Based on the X-ray CT data, the carbide particle size was assigned a log-normal distribution with parameters  $\mu$  and  $\sigma$  being 2.2738 and 0.5211, respectively. Beta distributions were assigned to the aspect ratios ( $\frac{b}{a}$  and  $\frac{c}{a}$ , where  $a$  is the length of major axis,  $b$  and  $c$  are lengths of minor axes of a best fit ellipsoid) of the particles. Both equiaxed and high aspect ratio particles were created. For equiaxed particles, both the aspect ratios  $\frac{b}{a}$  and  $\frac{c}{a}$  were assigned a beta distribution with shape parameters  $\alpha$  and  $\beta$  equal to 15.75 and 1.70, respectively. For high aspect ratio

particles, both the aspect ratios  $\frac{b}{a}$  and  $\frac{c}{a}$  were assigned a beta distribution with shape parameters  $\alpha$  and  $\beta$  equal to 4.9896 and 27.2253, respectively.

Based on the analysis of multiple EBSD scans, it was observed that cast MAR-M247 had a random texture. Hence, a random texture definition was assigned to the synthetic microstructures by assigning random orientations to grains in the microstructure. The grain size distribution, shown in Fig. 2b, was obtained from the EBSD scan, Fig. 2a. Since 3D synthetic microstructures were used in the current study, three main assump-

tions were made while transitioning the grain sizes obtained from 2D EBSD scans to create representative 3D microstructures. First, based on the aspect ratios of the grains calculated from multiple EBSD scans, it was assumed that the grains were equiaxed. Since the processing pedigree of the material, post casting, did not involve rolling or pressing. Second, based on the observation that the grain size distribution in a wide variety of metals and alloys follows a log-normal distribution (Feltham 1957), it was assumed that the grain size in the synthetic microstructures also followed a log-normal distribution. Finally, a stereological scaling factor,  $\frac{4}{\pi}$ , was applied to the 2D grain sizes obtained from the EBSD scan to get an estimate of the 3D grain size distribution. By comparing the grain size data obtained from a 3D microstructure (reconstructed from serial sectioning data) of a nickel-base superalloy, IN100, to the stereologically scaled 2D grain sizes obtained from individual EBSD scans, Groeber (2007) showed that there was <5% error between the two datasets. After stereologically scaling the 2D grain sizes obtained from EBSD scans (by a factor of  $\frac{4}{\pi}$ ), a 3D grain size was defined using a log-normal distribution with parameters  $\mu$  and  $\sigma$  being 4.7669 and 0.4925, respectively, with  $\mu$  and  $\sigma$  being the mean and standard deviation of the associated normal distribution of the logarithm of grain size parameter. Those parameters were obtained after fitting a log-normal distribution to the stereologically scaled 2D grain size distribution. The aforementioned statistical attributes were then input into the 'StatGenerator' toolbox of DREAM.3D to create three different instantiations of the microstructure of MAR-M247. The two-sample Kolmogorov-Smirnov (KS) method was employed (at 5% significance level) to test the null hypothesis which states that there is an equivalence between the stereologically scaled grain size distributions obtained from 2D EBSD scans and the grain size distributions within the synthetic microstructures generated by DREAM.3D. A synthetic microstructure was accepted as a MAR-M247 representative microstructure only after the two-sample KS test accepted the null hypothesis. In one of the synthetic microstructures generated, the 3D grain size distribution obtained from the microstructure was fit to a log-normal distribution. The fitting parameters for the log-normal distribution,  $\mu$  and  $\sigma$ , were 4.7344 and 0.5013, respectively, which are close to the aforementioned parameters of log-normal distribution that was fit to the stereologically scaled 2D grain size distribution obtained from EBSD scans.

For the purpose of this study, synthetic microstructures were created considering only the Hafnium and Tantalum rich MC carbide particles present at grain boundaries, and ignoring the Chromium-rich  $M_{23}C_6$  particles, due to the high frequency of cracking at MC particles. Further, the  $\gamma'$  precipitates were not explicitly modeled, such that the effect of the  $\gamma-\gamma'$  phase was homogenized. The interface between MC carbide particles and the  $\gamma-\gamma'$  matrix was assumed to be perfectly bonded, as de-cohesion between particles and matrix was never observed in microscopy images. Surface meshes of all the features (grains and carbides) comprising the two-phase polycrystalline microstructure were input into Gmesh (Geuzaine and Remacle 2009) to generate a tetrahedral volume mesh of the microstructure. This volume mesh was then input into an in-house finite element code, ScIFEi (Warner et al. 2016), to carry out the computationally-intensive simulations to solve for the heterogeneous stress and strain state within the microstructure.

### 3.3.1 Crystal plasticity framework

A CPFE framework was used to solve for the heterogeneous stress state within the polycrystalline microstructure by combining anisotropic elasticity with rate-dependent crystal plasticity kinetics. For the elastic behavior, individual grains representing the  $\gamma-\gamma'$  matrix were assigned cubic elastic constants  $C_{11}$ ,  $C_{12}$  and  $C_{44}$  equal to 258.6, 167.0, 125.0 GPa respectively (Kuhn and Sockel 1988), while the MC carbide particles were assigned isotropic elastic properties, with Young's modulus equal to 255 GPa (Li and Li 2010). This simplifying assumption precludes any dependence on crystallographic orientations within the carbides, but serves to reduce the number of variables for a tractable study. Poisson's ratio of the particles was assumed to be 0.33. No plasticity model was applied to the carbide particles, as it is well known that these particles are brittle. Rate-dependent crystal plasticity kinetics (flow rule and hardening law) were assigned for the homogenized  $\gamma-\gamma'$  matrix. Since the experiments were conducted at room temperature, it has been assumed that the plastic flow occurs only through dislocation glide on octahedral slip systems within the  $\gamma-\gamma'$  matrix, while cubic slip is not activated. The flow rule used for describing incremental slip on the octahedral slip systems is shown in Eq. 1

$$\dot{\gamma}^\alpha = \dot{\gamma}_0 \frac{\tau^\alpha}{g^\alpha} \left| \frac{\tau^\alpha}{g^\alpha} \right|^{\frac{1}{m}-1}, \quad (1)$$

where  $\dot{\gamma}^\alpha$  and  $\dot{\gamma}_0$  are the shear and reference shear rates of slip system  $\alpha$ , respectively,  $m$  is a shear rate sensitivity parameter,  $\tau^\alpha$  is the resolved shear stress acting on a slip system  $\alpha$ , and  $g^\alpha$  is critical resolved shear stress representing the delay in the onset of plastic deformation.

The slip resistance,  $\dot{g}^\alpha$ , shown in Eq. 2 evolves according to a gradient based evolution law obtained from combining the hardening laws given by Beaudoin et al. (2000) and Voce-Kocks relations (Kocks 1976)

$$\begin{aligned} \dot{g}^\alpha = & H_0 \frac{\beta^2 \mu^2 b}{2(g^\alpha - g_0^\alpha)} \sum_{k=1}^{N_{SS}} \sqrt{(\hat{n}_p^k : \Delta^T) (\Delta : \hat{n}_p^k)} |\dot{\gamma}^k| \\ & + G_0 \left( \frac{g_s^\alpha - g^\alpha}{g_s^\alpha - g_0^\alpha} \right) \sum_{k=1}^{N_{SS}} |\dot{\gamma}^k|, \end{aligned} \quad (2)$$

where  $g_0^\alpha$  and  $g_s^\alpha$  are the initial and saturation resolved shear strengths of slip system  $\alpha$ ,  $N_{SS}$  represents the number of slip systems,  $H_0$  and  $G_0$  are the direct hardening coefficients,  $\beta = \frac{1}{3}$  (Cerrone et al. 2015),  $b$  is the Burgers vector,  $\hat{n}_p$  is the slip plane normal,  $\mu$  an elastic constant equal to  $C_{44}$ ,  $\Delta$  is the measure of dislocation density and is calculated using the gradient of plastic deformation as shown in Eq. 3,

$$\Delta_{ij} = \epsilon_{jkl} F_{il,k}^p. \quad (3)$$

In addition to the elastic constants, there are 6 calibrated parameters ( $\dot{\gamma}_0$ ,  $m$ ,  $H_0$ ,  $G_0$ ,  $g_0^\alpha$  and  $g_s^\alpha$ ) in the crystal plasticity model used in the current framework. The parameters were iteratively tuned in order to fit the macroscopic stress strain curve of MAR-M247 at room temperature, obtained from Liao et al. (2010). The final calibration parameters of the crystal plasticity framework are shown in Table 2.

The CPFE simulations cannot resolve individual slip bands, and hence, cannot be used to model explicitly the interaction of slip bands with carbide particles, which were observed in microscopy images (shown in Fig. 6). However, using the CPFE framework, it is possible to study homogenized stress and strain fields within the microstructure. In a CPFE framework, stress and strain are interrelated through flow and hardening laws. The stress state within the features (grains

**Table 2** Calibrated parameters to fit the macroscopic stress strain curve of MAR-M247 at room temperature

Parameter	Value
$\dot{\gamma}_0$ ( $s^{-1}$ )	0.98
$m$	0.045
$H_0$ (MPa)	412.3
$G_0$ (MPa)	415.2
$g_0^\alpha$ (MPa)	320.2
$g_s^\alpha$ (MPa)	375.2

and carbides) was chosen as the metric to study which factors govern the propensity of driving crack incubation. Furthermore, since the MC carbide particles were assigned an isotropic linear elastic material property for which the principal strain axes coincides with principal stress axis, and as there exists a simplistic relation between stress and strain as per Hooke's law, to eliminate redundancy, we chose to only present principal stresses within the particles.

### 3.3.2 Polycrystal simulations

Three statistically representative polycrystal models of the MAR-M247 microstructure were generated to study the variation of particle stress state due to variation in neighboring microstructure. One of the microstructure models created using the workflow described in Sect. 4.3 is shown in Fig. 12. The microstructure model (shown in Fig. 12b, c) consists of 120 grains and 115 carbide particles, which were inserted at grain boundaries to be consistent with experimental observations. The finite element mesh of the microstructure model was discretized into 33,376,312 quadratic tetrahedral elements and contained 45,377,865 nodes. The boundary conditions applied on the microstructure model are described in Table 3. A strain of 1.5% was applied to the synthetic microstructures using displacement controlled loading. Each of the three simulations were run in parallel on 1000 processors using NASA's Pleiades supercomputing cluster for about 40 hours.

To better understand the fundamental observation that particles cracking appears stochastic, it is important to investigate the factors responsible for variation of stress state of the particles. For this purpose, four factors which serve to concentrate stress within the parti-

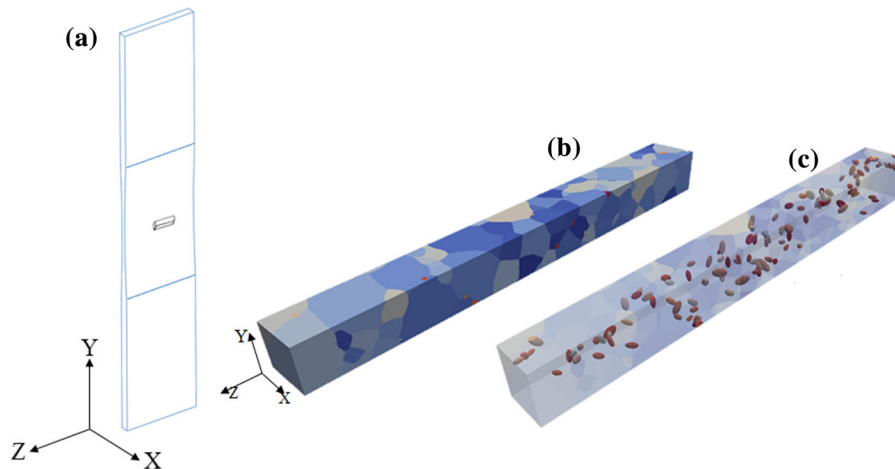


**Fig. 12** **a** 3D rendering of the specimen showing the coordinate axis and the location at which the microstructure volume is being modeled **b** a statistically representative polycrystal model of MAR-M247, with MC carbide particles at the grain boundaries. This particular microstructure has 235 features (120 grains

and 115 carbide particles) in a volume of  $200 \times 200 \times 2000 \mu\text{m}$ , with a resolution of  $2 \mu\text{m}$  per voxel. **c** Opacity of the same microstructure was adjusted to distinctly show all the carbide particles inserted at grain boundaries

**Table 3** Model boundary conditions

Boundary face	Boundary condition
-X	Fix X displacement
+X	Free
-Y	Fix Y displacement
+Y	Apply Y displacement
-Z	Fix Z displacement
+Z	Free

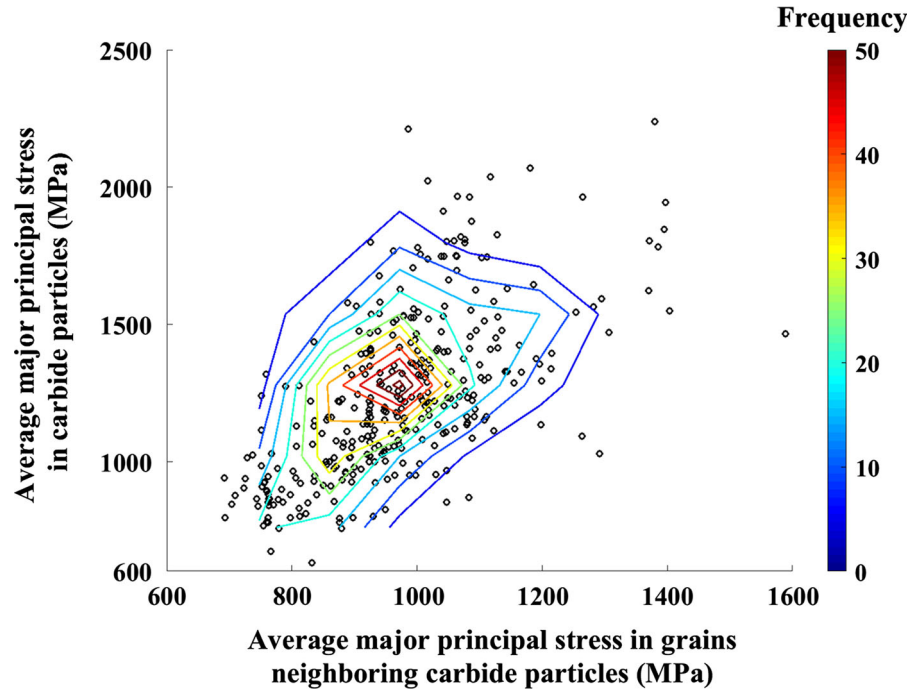
cles were considered in this study: (i) stress state of the grains surrounding the carbide particles; (ii) location of the particles w.r.t. the free surface; (iii) orientation of the particle w.r.t. loading direction; and (iv) grain boundary effects.

First, to study the influence of the stress state of the neighboring microstructure on the stress state of a carbide particle, average maximum principal stress was computed for all the particles, and for their corresponding grain neighbors. For each carbide particle, maximum principal stress was computed at every integration point in its discretized volume. The average value of the maximum principal stresses were then taken for each grain and carbide region separately. This homogenization method provides a convenient basis for investigating and illustrating the four stress-concentrating factors stated above. From three unique synthetic microstruc-

tures, the average stress state of 334 carbide particles, and the stress states of their immediate neighboring grains was collected, and the corresponding data obtained is illustrated in Fig. 13. Each data point in Fig. 13 corresponds to the average stress state of the carbide particle and to that of the volume occupied by the surrounding grains. There is an overall positive correlation between the average stress state of the neighboring grains and the average stress state of the carbide particles. In addition to the correlation, there is also a significant variation in the stress state of the carbide, for a given average stress state of the carbide neighborhood volume, occupied by its neighboring grains.

The homogenized average stress state of carbide particle provides no specific information regarding where or in which direction a crack would incubate. To study local heterogeneous stress concentration within carbide particles, maximum principal stress was plotted on the particle boundaries, see Fig. 14. For particles that reside within the bulk of the microstructure, Fig. 14a and b, a high concentration of maximum principal stress was observed at locations where the particle intersected with grain boundaries of neighboring grains. The development of stress concentration at the aforementioned location is driven due to a difference in lattice mismatch between the grains in addition to a significant differences in the elastic moduli between the grains and the carbide particle. With high maximum principal

**Fig. 13** Scatter plot overlaid on a density contour plot to show a correlation between the average value of maximum principal stress in carbide particles and average value of maximum principal stress in the grains neighboring each carbide particle. All the stress data was obtained at applied peak displacement when the macroscopic strain was 1.5%. Values on the *color bar* represents frequency, which is equivalent to the height of the 3D surface plot constructed from a bivariate histogram created on a rectangular grid, using the scatter data



stresses concentrated, the intersection sites of carbide particles with grain boundaries would be potential sites where cracks incubate within the carbide particle, and due to this the cracks within the particle can be favorable aligned with the grain boundaries. This is also in line with the microscopic observations made earlier.

In particles that intersect the free surface, Fig. 14c, d, stresses were observed to be most concentrated in regions within the particle close to the free surface, while showing a less pronounced stress concentration at its intersection with grain boundaries. The deformation and hence stress in carbide particles that reside completely within the bulk of the microstructure is constrained by grains neighboring the particle. But, particles that intersect with the free surface are relatively less constrained compared to particles completely within the bulk of the microstructure. Consequently, the carbide particles intersecting with the free surface are subject to statistically higher deformations specifically in regions close to the free surface, which lead to higher stresses in those regions, as shown in Fig. 14d.

Surface area data collected using microscopy images for both cracked and uncracked particles, shown in Fig. 4, statistically showed that particles with larger free surface area are more vulnerable to cracking. Hence, it was of interest to study if the stress state of the particle

would be influenced by the magnitude of its free surface area. For this purpose, 24 carbide particles that intersect with the free surface of the microstructure were considered from the three virtual microstructures used in this study. The free-surface area of the 24 particles was calculated from their respective surface meshes. In each surface mesh, the facets that lie on the free surface were filtered out and the overall free surface area was calculated by summing up the areas of individual free-surface facets. Following the calculation of free-surface area, the average maximum principal stress was obtained for each of the 24 particles. The average maximum principal stress was plotted against the free-surface area of the particles, as shown in Fig. 15 using an error bar plot, where the error bars represent standard deviation in a particular bin. The variance in stress states of particles arise from various factors including heterogeneity neighboring microstructure and geometric attributes of the carbide particles (orientation, aspect ratio etc.). Overall, a positive correlation was observed between the average maximum principal stress and the free-surface area of particles, implying that increased stress concentration is one of influential factors behind the observed higher propensity of crack incubation in particles with large free surface area.

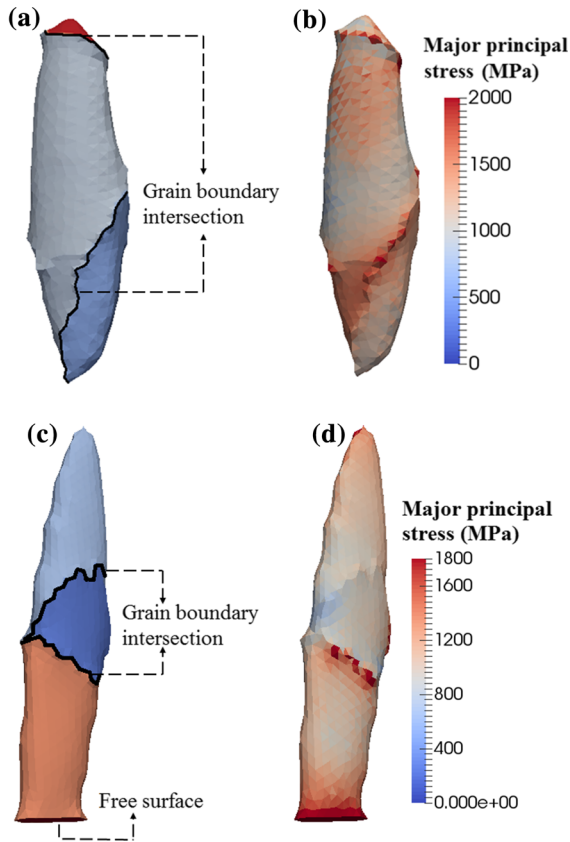


**Fig. 14** **a** 3D rendering of a carbide particle present within the bulk of the microstructure, colored in such a way that each color represent a different grain neighbor. The intersection of the particle's surface with grain boundaries is shown using a *thick black line*, **b** maximum principal stress value plot for the particle, **c** 3D rendering of a carbide particle that intersects with the free surface, colored in such a way that each color represent a different grain neighbor. The intersection of the particle's surface with grain boundaries is shown using a *thick black line*, **d** maximum principal stress value plot for the particle. The visualizations of the maximum principal stress states in both the carbide particles were obtained at applied peak displacement when the macroscopic strain was 1.5%

In addition to the carbide neighborhood and free surface effects, the influence of particle alignment with respect to the load direction on the stress state of the particle was also investigated. For the purpose of this study, the orientation of a particle with the applied load was calculated as the angle between the particle major axis, determined by a best fit ellipsoid, and the applied load direction. Orientations were obtained for all the carbide particles from three microstructures, except for the ones which intersect with the surfaces on which boundary conditions were applied. The average maxi-

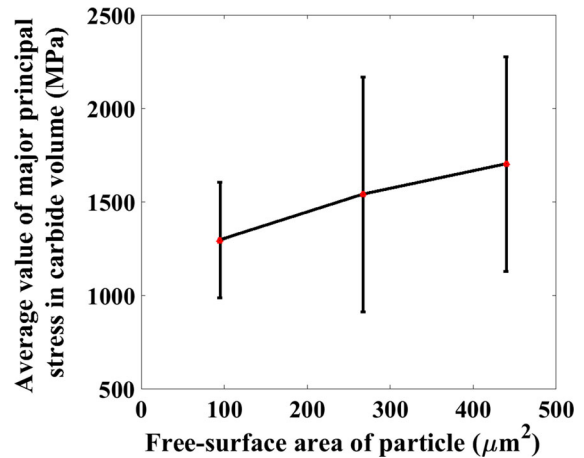


**Fig. 15** Average value of maximum principal stress in carbide particles grouped by free surface area of particles. Error bars on the plot represent standard deviation. The stress data for all the particles was obtained at applied peak displacement when the macroscopic strain was 1.5%

imum principal stress in the particles was plotted against the orientation of the particles, see Fig. 16. It can be inferred from the plot that particles with their major axis aligned closely with the tensile load axis experience higher stresses relative to those particles whose major axis is perpendicular to the load axis. MC carbide particles which belong to the latter category can significantly improve the fatigue resistance and hence contribute towards improving the fatigue life of the material.

CPFE analysis helped gain insights into the various factors that influence the stress state of carbide particles. Based on the analysis, it was shown that although the free-surface area of particles is significant (as shown in Fig. 15), the variability of the stress state of the particles is also affected by: (i) the geometric alignment of the particles with respect to the loading direction, (ii) stress concentrations developed by the interaction of particles with grain boundaries and free-surface (as shown in Fig. 14) and (iii) the variability in the local microstructure surrounding the carbide particles (as shown in Fig. 13). In addition to these first-order direct correlations, determining the covariance matrix would help ascertain the second-order effects, which would be a beneficial extension of the current work.

Extension of this work toward prediction of carbide particle cracking would require validation of the assumption that there is a direct relationship between the carbide particle stress state and likelihood of crack

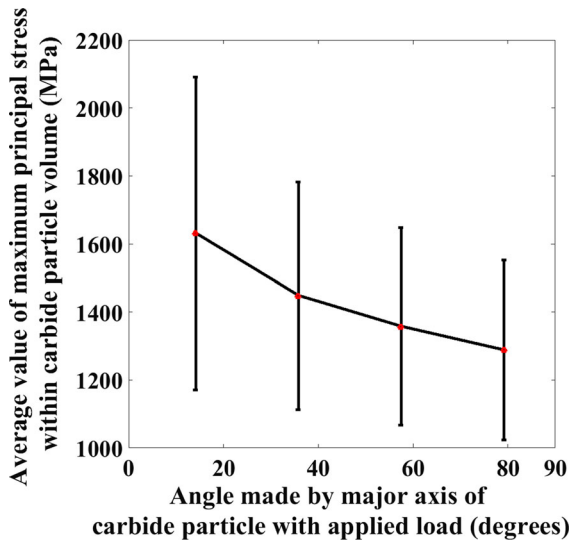


**Fig. 16** Average value of maximum principal stress in carbide particles grouped by the angle made by the major axis of particles with the load direction. The stress data for all the particles was obtained at applied peak displacement when the macroscopic strain was 1.5%

incubation. Such a validation would require either a direct measurement of carbide particle stress state (via strain measurement and assumption of linear elasticity) or replicating the 3D geometry of the carbide particles and computing stress (via CPFEM). If valid, a comparison of cracked and intact carbide particles would effectively calibrate a particle strength to be used for prediction.

#### 4 Conclusions

The following conclusions are drawn from this work:

- Fatigue cracks incubated extensively at large Hafnium/Tantalum rich MC carbide particles, when MAR-M247 was subject to low cycle fatigue at room temperature.
- Analysis of secondary electron images showed that the free-surface area of cracked particles was approximately three times that of the uncracked particles. Further, it was determined that the cracks aligned nearly perpendicular to the loading direction in particles with aspect ratios  $<3$ , the cracks predominantly aligned with the major axis, in particles with high aspect ratios.
- Through forward-scattered electron imaging, it was observed that a significant number of slip bands

interacted with a large number of carbide particles which cracked. Fewer particles were still intact upon the interaction of slip bands.

- Microscopy analysis showed that a large life-limiting crack grew crystallographically, even when spanning the length of multiple grains. HREBSD analysis showed that the crack grew along slip bands of two active slip systems.
- Crystal plasticity finite element (CPFEM) simulations that were run using virtual microstructures of MAR-M247 showed that there are four major contributing factors which influence the stress state of the carbide particles. (i) A strong positive correlation was observed between the average maximum principal stresses of the carbide particles and the average maximum principal stress within the grains neighboring the carbide. (ii) An inverse correlation was observed between the angle made by major axis of carbide particles with the load direction and their average maximum principal stress. Particles with their major axis aligned closely with the tensile axis experienced higher stresses compared to the particles whose major axis was perpendicular to the tensile axis. (iii) For particles which intersect with the free surface, the magnitude of their free surface area has a direct correlation with the average maximum principal stress within the particles and the regions of particles close to the free surface experienced high principal stresses. (iv) Finally, high stress concentrations were observed in regions where the carbide particle intersected with the grain boundaries.

**Acknowledgements** This project was funded by the NASA Engineering and Safety Center. SY and MDS acknowledge support by the National Institute of Aerospace (grant number 2712-001).

#### References

- Beaudoin AJ, Acharya A, Chen SR et al (2000) Consideration of grain-size effect and kinetics in the plastic deformation of metal polycrystals. *Acta Mater* 48:3409–3423. doi:10.1016/S1359-6454(00)00136-1
- Boismier DA, Sehitoglu H (1990) Thermo-mechanical fatigue of Mar-M247: part 1—experiments. *J Eng Mater Technol Trans ASME* 112:68. doi:10.1115/1.2903189
- Bor HY, Chao CG, Ma CY (1999) The effects of Mg microaddition on the mechanical behavior and fracture mechanism of MAR-M247 superalloy at elevated tempera-



- tures. *Metall Mater Trans A* 30:551–561. doi:[10.1007/s11661-999-0047-3](https://doi.org/10.1007/s11661-999-0047-3)
- Bowman R, Ritzert F, Freedman M (2004) Evaluation of candidate materials for a high-temperature stirling convertor heater head. *Space technology and applications international forum*. Melville, NY, pp 821–828
- Bozek JE, Hochhalter JD, Veilleux MG et al (2008) A geometric approach to modeling microstructurally small fatigue crack formation: I. Probabilistic simulation of constituent particle cracking in AA 7075–T651. *Model Simul. Mater Sci Eng* 16:65007. doi:[10.1088/0965-0393/16/6/065007](https://doi.org/10.1088/0965-0393/16/6/065007)
- Brindley KA, Kirka MM, Fernandez-Zelaia P, Neu RW (2015) Thermomechanical fatigue of Mar-M247: Extension of a unified constitutive and life model to higher temperatures. *J Eng Mater Technol Trans ASME*. doi:[10.1115/1.4029908](https://doi.org/10.1115/1.4029908)
- Castelluccio GM, McDowell DL (2012) Effect of annealing twins on crack initiation under high cycle fatigue conditions. *J Mater Sci* 48:2376–2387. doi:[10.1007/s10853-012-7021-y](https://doi.org/10.1007/s10853-012-7021-y)
- Cerrone A, Stein C, Pokharel R et al (2015) Implementation and verification of a microstructure-based capability for modeling microcrack nucleation in LSHR at room temperature. *Model Simul Mater Sci Eng* 23:35006. doi:[10.1088/0965-0393/23/3/035006](https://doi.org/10.1088/0965-0393/23/3/035006)
- Chen J, Lee J, Jo C et al (1998) MC carbide formation in directionally solidified MAR-M247 LC superalloy. *Mater Sci Eng A* 247:113–125. doi:[10.1016/S0921-5093\(97\)00761-2](https://doi.org/10.1016/S0921-5093(97)00761-2)
- Feltham P (1957) Grain growth in metals. *Acta Metall* 5:97–105. doi:[10.1016/0001-6160\(57\)90136-0](https://doi.org/10.1016/0001-6160(57)90136-0)
- Gell M, Leveran GR (1968) The fatigue of the nickel-base superalloy Mar-M200 in single crystal and columnar-grained forms at room temperature. *Trans TMS-AIME* 242:1869–1879
- Geuzaine C, Remacle JF (2009) Gmsh: a 3-D finite element mesh generator with built-in pre- and post-processing facilities. *Int J Numer Methods Eng* 79:1309–1331. doi:[10.1002/nme.2579](https://doi.org/10.1002/nme.2579)
- Groeber MA (2007) Development of an automated characterization-representation framework for the modeling of polycrystalline materials in 3D. Ph.D. thesis, Ohio State University, Columbus, Ohio
- Groeber M, Jackson M (2014) DREAM.3D: a digital representation environment for the analysis of microstructure in 3D. *Integr Mater Manuf Innov* 3:5. doi:[10.1186/2193-9772-3-5](https://doi.org/10.1186/2193-9772-3-5)
- Janowski GM (1985) The effect of tantalum on the structure/properties of two polycrystalline nickel-base superalloys: B-1900+Hf and MAR-M247, NASA Contractor Report 174847
- Jiang J, Yang J, Zhang T et al (2015) On the mechanistic basis of fatigue crack nucleation in Ni superalloy containing inclusions using high resolution electron backscatter diffraction. *Acta Mater*. doi:[10.1016/j.actamat.2015.06.035](https://doi.org/10.1016/j.actamat.2015.06.035)
- Kamış T, Bağcı S, Tütüncü HM et al (2011) Ab initio calculation of phonons in bulk HfC and the HfC(001)(1 × 1) surface. *Philos Mag* 91:946–957. doi:[10.1080/14786435.2010.536177](https://doi.org/10.1080/14786435.2010.536177)
- Karamched PS, Wilkinson AJ (2011) High resolution electron back-scatter diffraction analysis of thermally and mechanically induced strains near carbide inclusions in a superalloy. *Acta Mater* 59:263–272. doi:[10.1016/j.actamat.2010.09.030](https://doi.org/10.1016/j.actamat.2010.09.030)
- Kartal ME, Kiwanuka R, Dunne FPE (2014) Determination of sub-surface stresses at inclusions in single crystal superalloy using HR-EBSD, crystal plasticity and inverse eigenstrain analysis. *Int J Solids Struct* 67–68:27–39. doi:[10.1016/j.ijsolstr.2015.02.023](https://doi.org/10.1016/j.ijsolstr.2015.02.023)
- Kaufman M (1984) Properties of Cast Mar-M-247 for Turbine Blisk Applications. In: *Superalloys 1984* (fifth international symposium). TMS, pp 43–52
- Kocks F (1976) Laws for work-hardening and low-temperature creep. *J Eng Mater Technol* 98:76–85. doi:[10.1115/1.3443340](https://doi.org/10.1115/1.3443340)
- Kotval PS, Venables JD, Calder RW (1972) The role of hafnium in modifying the microstructure of cast nickel-base superalloys. *Metall Trans* 3:457–462. doi:[10.1007/BF02642049](https://doi.org/10.1007/BF02642049)
- Kuhn HA, Sockel HG (1988) Comparison between experimental determination and calculation of elastic properties of nickel-base superalloys between 25 and 1200 °C. *Phys Status Solidi* 110:449–458. doi:[10.1002/pssa.2211100217](https://doi.org/10.1002/pssa.2211100217)
- Li G, Li G (2010) Microstructure and mechanical properties of hafnium carbide coatings synthesized by reactive magnetron sputtering. *J Coatings Technol Res* 7:403–407. doi:[10.1007/s11998-009-9225-x](https://doi.org/10.1007/s11998-009-9225-x)
- Liao J-H, Bor H-Y, Chao C-G, Liu T-F (2010) Effects of rhenium on microstructure and phase stability of MAR-M247 Ni-base fine-grain superalloy. *Mater Trans* 51:810–817. doi:[10.2320/matertrans.M2009331](https://doi.org/10.2320/matertrans.M2009331)
- MacSleyné JP, Simmons JP, De Graef M (2008) On the use of moment invariants for the automated analysis of 3D particle shapes. *Model Simul Mater Sci Eng* 16:45008. doi:[10.1088/0965-0393/16/4/045008](https://doi.org/10.1088/0965-0393/16/4/045008)
- Margolin H (1998) Polycrystalline yielding—perspectives on its onset. *Acta Mater* 46:6305–6309. doi:[10.1016/S1359-6454\(98\)00227-4](https://doi.org/10.1016/S1359-6454(98)00227-4)
- Miao J, Pollock TM, Wayne Jones J (2009) Crystallographic fatigue crack initiation in nickel-based superalloy René 88DT at elevated temperature. *Acta Mater* 57:5964–5974. doi:[10.1016/j.actamat.2009.08.022](https://doi.org/10.1016/j.actamat.2009.08.022)
- Murakami Y, Endo M (1994) Effects of defects, inclusions and inhomogeneities on fatigue strength. *Int J Fatigue* 16:163–182. doi:[10.1016/0142-1123\(94\)90001-9](https://doi.org/10.1016/0142-1123(94)90001-9)
- Nathal MV, Maier RD, Ebert LJ (1982) The influence of cobalt on the tensile and stress-rupture properties of the nickel-base superalloy MAR-M247. *Metall Trans A* 13:1767–1774. doi:[10.1007/BF02647832](https://doi.org/10.1007/BF02647832)
- Neumann P (1999) Analytical solution for the incompatibility stresses at twin boundaries in cubic crystals. In: *Fatigue*. Beijing, pp 107–114
- Przybyla C, Prasannavenkatesan R, Salajegheh N, McDowell DL (2010) Microstructure-sensitive modeling of high cycle fatigue. *Int J Fatigue* 32:512–525. doi:[10.1016/j.ijfatigue.2009.03.021](https://doi.org/10.1016/j.ijfatigue.2009.03.021)
- Ruggles TJ, Fullwood DT, Kysar JW (2016) Resolving geometrically necessary dislocation density onto individual dislocation types using EBSD-based continuum dislocation microscopy. *Int J Plast* 76:231–243. doi:[10.1016/j.iplas.2015.08.005](https://doi.org/10.1016/j.iplas.2015.08.005)
- Salajegheh N, Prasannavenkatesan R, McDowell DL et al (2014) Finite element simulation of shielding/intensification effects of primary inclusion clusters in high strength steels under fatigue loading. *J Eng Mater Technol* 136:31003. doi:[10.1115/1.4027380](https://doi.org/10.1115/1.4027380)

- Sangid MD, Maier HJ, Sehitoglu H (2011c) The role of grain boundaries on fatigue crack initiation—an energy approach. *Int J Plast* 27:801–821. doi:[10.1016/j.ijplas.2010.09.009](https://doi.org/10.1016/j.ijplas.2010.09.009)
- Sangid MD, Maier HJ, Sehitoglu H (2011b) A physically based fatigue model for prediction of crack initiation from persistent slip bands in polycrystals. *Acta Mater* 59:328–341. doi:[10.1016/j.actamat.2010.09.036](https://doi.org/10.1016/j.actamat.2010.09.036)
- Sangid MD, Maier HJ, Sehitoglu H (2011a) An energy-based microstructure model to account for fatigue scatter in polycrystals. *J Mech Phys Solids* 59:595–609. doi:[10.1016/j.jmps.2010.12.014](https://doi.org/10.1016/j.jmps.2010.12.014)
- Schneider CA, Rasband WS, Eliceiri KW (2012) NIH Image to ImageJ: 25 years of image analysis. *Nat Methods* 9:671–675. doi:[10.1038/nmeth.2089](https://doi.org/10.1038/nmeth.2089)
- Schreiber JG, Thieme LG (2008) GRC supporting technology for NASA's Advanced Stirling Radioisotope Generator (ASRG). *AIP Conf Proc* 969:582–592. doi:[10.1063/1.2845018](https://doi.org/10.1063/1.2845018)
- Sehitoglu H, Boismier DA (1990) Thermo-mechanical fatigue of Mar-M247: part 2—life prediction. *J Eng Mater Technol* 112:80. doi:[10.1115/1.2903191](https://doi.org/10.1115/1.2903191)
- Shenoy MM, Kumar RS, McDowell DL (2005) Modeling effects of nonmetallic inclusions on LCF in DS nickel-base superalloys. *Int J Fatigue* 27:113–127. doi:[10.1016/j.ijfatigue.2004.06.008](https://doi.org/10.1016/j.ijfatigue.2004.06.008)
- Šmíd M, Horník V, Hutař P et al (2016) High cycle fatigue damage mechanisms of MAR-M 247 superalloy at high temperatures. *Trans Indian Inst Met* 69:393–397. doi:[10.1007/s12666-015-0817-0](https://doi.org/10.1007/s12666-015-0817-0)
- Šmíd M, Kunz L, Hutař P, Hrbáček K (2014) High cycle fatigue of nickel-based superalloy MAR-M 247 at high temperatures. *Procedia Eng* 74:329–332. doi:[10.1016/j.proeng.2014.06.273](https://doi.org/10.1016/j.proeng.2014.06.273)
- Szczotok A, Rodak K (2012) Microstructural studies of carbides in MAR-M247 nickel-based superalloy. *IOP Conf Ser Mater Sci Eng* 35:12006. doi:[10.1088/1757-899X/35/1/012006](https://doi.org/10.1088/1757-899X/35/1/012006)
- Szczotok A, Szala J, Cwajna J, Hetmańczyk M (2006) Selection of etching methods of primary carbides in MAR-M247 nickel-base superalloy for computer-aided quantitative metallography. *Mater Charact* 56:348–354. doi:[10.1016/j.matchar.2005.10.011](https://doi.org/10.1016/j.matchar.2005.10.011)
- Warner JE, Bomarito GF, Hochhalter JD (2016) Scalable implementation of finite elements by NASA \_ Implicit (ScIFEi), NASA/TM—2016–219180. Hampton, Virginia
- Wawro SW (1982) MC carbide structures in Mar-M247, NASA Contractor Report 167892
- Wood JG, Carroll C, Matejczyk D, Penswick L (2005) Advanced 80 We stirling convertor phase II development progress. In: 3rd International energy conversion engineering conference. doi:[10.2514/6.2005-5559](https://doi.org/10.2514/6.2005-5559)
- Yeratapally SR, Glavicic MG, Hardy M, Sangid MD (2016) Microstructure based fatigue life prediction framework for polycrystalline nickel-base superalloys with emphasis on the role played by twin boundaries in crack initiation. *Acta Mater*. doi:[10.1016/j.actamat.2016.01.038](https://doi.org/10.1016/j.actamat.2016.01.038)
- Zhang J, Prasannavenkatesan R, Shenoy MM, McDowell DL (2009) Modeling fatigue crack nucleation at primary inclusions in carburized and shot-peened martensitic steel. *Eng Fract Mech* 76:315–334. doi:[10.1016/j.engfractmech.2008.10.011](https://doi.org/10.1016/j.engfractmech.2008.10.011)
- Zhang T, Collins DM, Dunne FPE, Shollock BA (2014) Crystal plasticity and high-resolution electron backscatter diffraction analysis of full-field polycrystal Ni superalloy strains and rotations under thermal loading. *Acta Mater* 80:25–38. doi:[10.1016/j.actamat.2014.07.036](https://doi.org/10.1016/j.actamat.2014.07.036)
- Zhang T, Jiang J, Britton B et al (2016) Crack nucleation using combined crystal plasticity modelling, high-resolution digital image correlation and high-resolution electron backscatter diffraction in a superalloy containing non-metallic inclusions under fatigue. *Proc R Soc A Math Phys Eng Sci* 472:20150792. doi:[10.1098/rspa.2015.0792](https://doi.org/10.1098/rspa.2015.0792)
- Zhang T, Jiang J, Shollock BA et al (2015) Slip localization and fatigue crack nucleation near a non-metallic inclusion in polycrystalline nickel-based superalloy. *Mater Sci Eng A* 641:328–339. doi:[10.1016/j.msea.2015.06.070](https://doi.org/10.1016/j.msea.2015.06.070)